Ground-based measurements of local cloud cover

Abel Antônio Silva, Mariza Pereira de Souza Echer

Meteorol Atmos Phys (2013) 120:201–212
DOI 10.1007/s00703-013-0245-9

ORIGINAL PAPER

Ground-based measurements of local cloud cover

Abel Antônio Silva · Mariza Pereira de Souza Echer

Received: 4 July 2012 / Accepted: 7 March 2013 / Published online: 20 March 2013

Abstract Clouds are believed to reflect temporal climate changes through variations in their amounts, characteristics, and occurrence. In addition, they reflect both weather and climate in a region. In this work, a methodology to determine the local cloud cover (LCC) is proposed using sky images obtained from a ground-based instrument. Three years of sky images from an urban, tropical site were obtained and analyzed through that methodology. Monthly average LCC varied from 3 to 96 %, while seasonal average values were 68 % for summer, 54 % for spring, 46 % for fall, and 23 % for winter. LCC results show a clear seasonal dependence and a fair agreement ($r^2 = 0.72$) with satellite data, which typically underestimate the cloud cover in relation to LCC. Our analysis also suggests the possibility of a measurable link between LCC and natural events like the El Niño Southern Oscillation.

1 Introduction

Clouds are the main atmospheric factor modulating the surface incidence of solar radiation. Fundamentally, not only the precipitation, but also the incidence of solar radiation on earth's surface depends on clouds. Clouds are responsible for a major part of atmospheric albedo—23 % of the total short wave radiation (0–4 μm) reaching the top of the atmosphere. In addition, clouds are able to absorb long wave radiation emitted by the earth (8–12 μm). Clouds' optical thickness depends on optical properties and contents of water. The combined effect albedo-absorption is called cloud forcing, which has strong implications on climate and the solar energy budget for the biosphere (Hobbs 1993; Salby 1996).

According to a general definition, clouds are formed by the association of many small water droplets resulting from the accumulation of condensed water on cloud condensation nuclei of hydrophilic material (e.g., the sulfates) or also from the aggregation of ice crystals (Houze 1993; Kiehl 1994; Mason 1972). Nonetheless, despite this formal and useful scientific definition of what a cloud is, a more comprehensive definition has been required since the recent studies have suggested clouds can extend beyond their visible domains (Chiu et al. 2009; Koren et al. 2007; Jeong and Li 2010). In addition, many particle ensembles in the atmosphere can misleadingly be seen as a cloud. Visually, space and temporal variations in clouds turn the determination of cloud cover and cloud type into complex issues. Therefore, the definition and detection of clouds represent a hard task especially for remote observation.

Variations in cloud cover reflect the weather and climate of a region. Thus, it is reasonable to suppose environmental changes being evidenced by variations in the amounts, characteristics, and occurrence of clouds (Carslaw et al. 2002; Singh et al. 2011). It is believed that global climate change will yield variations in cloud cover around the world in the coming decades. Model simulations have stated a 3 % reduction at low latitudes (<30°), although there is a considerable margin of uncertainty in this figure

Responsible editor: C. Simmer.

A. A. Silva (✉)
Instituto de Estudos Avançados, Rod. dos Tamoios km 5.5, Torrão de Ouro II, São José dos Campos, SP, CEP 12228-001, Brazil
e-mail: abel@ieav.cta.br

M. P. de Souza Echer
Instituto Nacional de Pesquisas Espaciais, Av. dos Astronautas 1758, Jd. Granja, São José dos Campos, SP, CEP 12227-010, Brazil

(McKenzie et al. 2011). This is one of the main reasons to observe clouds globally. Therefore, it is necessary to measure the characteristics and amounts of clouds through systematic routines.

The observation of clouds is an old meteorological activity developed by human observers. However, the visual inspection of clouds is rather subjective bearing intrinsic uncertainty and bias that may lead to unreliable results. For the study of climate change and validation of satellite methods, the information on clouds from such a method is quite questionable. Recently, cloud observations have been improved by the use of automatic ground-based and orbital imagers. From the ground, the cloud cover corresponds to the fraction of sky covered by clouds as an angular concept that is quantitatively equal to the ratio between the sky solid angle covered by clouds and the total solid angle of the sky hemisphere. An inherent systematic bias (the perspective effect) is present in this concept through the dependence of the cloud cover amount on the cloud's elevation angle. On the other hand, for an instrument carried by a satellite orbiting the earth, the amount of clouds covering a fraction of land is indicated by the cloud fraction (CF) parameter (Stammes et al. 2008). In this case, the cloud observation is significantly free from the perspective effect due to the intrinsic geometry of hundreds of kilometers between the clouds and the orbital imager. Therefore, cloud cover and CF are concepts leading not necessarily to the same amounts of cloud cover.

Some ground-based automatic imagers have been in operation around the world for the determination and assessment of cloud cover (Cazorla et al. 2008; Holle and MacKay 1975; Long et al. 2006; Kazantzidis et al. 2012; Mantelli Neto et al. 2010; Martins et al. 2003; Pfister et al. 2003; Sabburg and Long 2004; Souza-Echer et al. 2006). Images from such devices are yielded by digital cameras facing directly the sky through wide-angular lens or indirectly through the reflection of sky images on a mirror. Alternatively, satellites have released CF values from experiments, such as the Ozone Monitoring Instrument (OMI) onboard the Aura Satellite launched by the National Aeronautics and Space Administration (NASA) (Levelt et al. 2006; Schoeberl et al. 2004; Stammes et al. 2008). CF is not a direct cloud cover measurement, but a result drawn from algorithms that take into account the reflectance of clouds, the atmosphere, and the ground. The reflectance is affected by terrestrial interferences like snowy and sandy surfaces. Hence, comparisons with cloud cover measurements from ground-based equipment are essential to validate satellite data. However, despite the initiative of many groups around the world developing instruments to measure the cloud cover, a standardized and wide applicable routine to obtain it through automatic devices has not yet been achieved. The development of such a routine would improve the studies on cloud cover and cloud characteristics.

In this work, we describe a methodology to obtain the local cloud cover (an hourly running average value obtained at a rate of 1 per minute) for a site from images taken by a ground-based platform. The methodology was applied to 3 years of data from an urban, tropical site in the Southern Hemisphere. The local cloud cover and its variations were depicted and a comparison with satellite data was also provided. The analysis suggests these variations could be caused by natural events like the El Niño Southern Oscillation (ENSO). Therefore, site and instruments are described in the next section, which is followed by a section for the presentation of the proposed methodology (routine) to obtain the local cloud cover. The procedure to operate the imager and to analyze the data drawn from it is presented in the Methodology section. The section of Results and discussion shows the obtained results of local cloud cover for the site, discusses these data in relation to an ENSO event, and makes a comparison with satellite data. Then, conclusions pointed out the main achievements in this work.

2 Site and instruments

2.1 Site description

Cloud cover measurements were obtained in Belo Horizonte (BH, 19.92°S, 43.94°W, 858 m a.s.l., 331 km^2, Brazil), the center of the 3rd largest Brazilian metropolitan area inhabited by 5.4 million people. As a municipality, BH has a fleet over 1.2 million vehicles featured with catalytic converter devices and electronic injection engines. Commercial and industrial activities predominate in the region. In terms of environment, it is settled in a hilly area in the south-eastern part of the country between the savanna (Cerrado) and the remains of the Atlantic forest (Mata Atlântica), featuring a tropical climate of altitude (it means milder weather due to site's altitude) with dry season from May to September and rainy one from November to March. Huge amounts of biomass burning smoke are blown into the city in the dry season. Seasons can be split as in the following: summer is December, January, and February; fall is March, April, and May; winter is June, July, and August; and spring is September, October, and November.

2.2 The Total Sky Imager

A Total Sky Imager 440A (TSI, Yankee Environmental Systems, Inc., Turners Falls, USA) comprises a digital camera facing down a rotating spherical mirror on which a

sky image reflection is photographed. A black strip is attached to the mirror in order to avoid direct reflection of sunbeams into the camera. Each snapshot results in a 24-bit color Joint Photographic Experts Group (JPEG) image with 352 × 288 pixel resolution amounting to around 35 kbytes. However, the ensemble formed by the digital camera + the spherical mirror does not produce high quality images, and tiny details from both sky and clouds become generally undetectable. A program (the TSI routine), provided by the manufacturer to be setup in a personal computer, controls the TSI and processes the obtained images to determine the cloud cover.

The image analysis by the TSI routine is based on the RGB (Red, Green, Blue) code. Each image pixel has R and B signals, and a red to blue signal ratio (the R/B ratio) is associated with the pixel (Long et al. 2006; Pfister et al. 2003). Fundamentally, a specific value for this ratio is chosen by the TSI operator as a limit for classifying a pixel as cloudy or cloud-free: R/B ratios below the limit represent cloud-free, bluish sky pixels, while R/B ratios above that limit refer to cloudy pixels. The sky perception by a TSI operator is a preponderant aspect in the determination of that specific R/B ratio limit.

Some studies use the term "clear sky" meaning "cloud-free", but only the latter is used here because it fits our reasoning best. In fact, a clear sky can completely diverge from a cloud-free one if the latter has considerable amounts of particle matter (aerosols) (Li and Tang 2008). On the other hand, a successful application of the TSI routine depends hugely on the intensity of light in the atmosphere (the sky illumination), which depends on the solar zenith angle (SZA), the cloud cover, cloud type, and the aerosol load in the atmosphere. It is worth mentioning that aerosols and clouds have a close relationship that sometimes makes the identification of clouds troublesome (Loeb and Schuster 2008). Moreover, there is another intrinsic aspect to complicate the scene formed by clouds and aerosols: the R and B signals depend on both the pixel relative position to the sun and the SZA.

Originally, the cloud cover determination by a human observer is depicted dividing the sky in tenths or oktas. Except for cloud-free and overcast scenarios, it is reasonable to ascribe at least a 10 % uncertainty to the measurements of cloud cover (Jeong and Li 2010; Sabburg and Long 2004). For a ground-based instrument, such as TSI, the cloud cover uncertainty for just one image depends on: (1) the amount of sky obstructed by the TSI components (the black strip on the mirror, the digital camera housing, and the camera's arm support); (2) the amount of pixels in the outer edge of an image (a peripheral circular area) to be rejected during the image processing by the TSI routine; and, (3) the difficult to delimit borders and thin parts of clouds, which seems to be one of the most critical aspects here. In fact, recent studies have shown that the cloud's borderline is a territory not clearly identified that can extend to distances comparable to the cloud's visible domains, especially when aerosols are present (Chiu et al. 2009; Jeong and Li 2010; Koren et al. 2007; Loeb and Schuster 2008). The interference of clouds in the atmosphere also occurs in wavelengths below and above the visible range of the electromagnetic spectrum. Therefore, the real size and territory of influence of a cloud depend on the radiation range used to observe it. In this study, all observations refer exclusively to the visible range.

2.2.1 *The TSI routine parameters based on R/B ratios for pixel classification*

The determination of a TSI image pixel as cloudy or cloud-free depends on the crucial and adequate setting of the R/B ratio limits to produce two TSI routine parameters: (1) the clear/thin parameter; and (2) the thin/opaque parameter. Pixels with R/B ratio below the clear/thin parameter are cloud free, while pixels with R/B ratio above this limit are cloudy. The clear/thin parameter depends on the amount of aerosols in the atmosphere. Similarly, cloudy pixels can be sub-classified as either thin or opaque depending on the thin/opaque parameter. The summation of thin and opaque portions makes the cloud cover. Therefore, these parameters work as thresholds and must be selected in order to provide the best match between the processed TSI images and the sky scene to be seen by an observer. However, the determination of such parameters is a bit arbitrary, since it is purely based on the experience and perception of the observer. The thin/opaque parameter is especially critical due to its highly imprecise character. The identification of borders and thin parts of clouds depends not only on the subjective interpretation of the observer, but also on effects like (1) the low level of illumination in some parts of the sky produced by clouds obstructing the sun, and (2) the presence of aerosol plumes which can misleadingly be seen as the thin parts of a cloud.

2.2.2 *Drawbacks in the TSI images*

The Total Sky Imager is an outstanding instrument. However, as a technological product, TSI images contain some troublesome effects from natural and artificial sources. The perspective effect misleadingly yields a false impression of cloud cover at large zenith angles (ZA). Another depreciating effect is the image distortion yielded by the TSI mirror also at large ZA. Although there is no suitable correction for the perspective effect, there is a procedural correction for the image distortion produced by the mirror′s geometry. The maximum distortion from a TSI mirror reaches around 8 % at ZA ≈ 50° (Long et al. 2006).

Another troublesome effect related to large ZA is the glare (or whitening) produced by intense sunlight scattering. Although the scattering of sunlight by atmospheric gases varies with λ^{-4} because molecules are much smaller than the radiation wavelength λ, the scattering by cloud droplets and aerosol particles depends approximately on λ^{-v} with $v < 4$. Consequently, light from clouds and aerosol plumes tends to be pale-whitened due to a lower order of dependence of the radiation scattering on the wavelength. Because of that, wide areas around the sun can be erroneously taken as cloudy by the TSI routine at larger ZA (>60°) and/or under considerable aerosol load. There is not yet an efficient method for completely differing clouds from aerosols using only the R/B ratio in this case (Long 2010). Therefore, the pale-whitened area must be cut out during the TSI routine application to process the TSI images.

2.3 The Ozone Monitoring Instrument

The Ozone Monitoring Instrument (OMI) is a Dutch-Finnish instrument on board the NASA's Aura satellite launched on July 15 2004 at 705 km sun-synchronous polar orbit, 98° inclination, and equator-crossing local time at 13:45 ± 15 min (Levelt et al. 2006). OMI data have been released since October 2004. A two-dimensional Charge Couple Device measures the ultraviolet–visible radiation (270–500 nm with ≈0.5 nm spectral resolution) from the sun and reflected from earth in swathes of 2,600 km (115°) perpendicular to the satellite flight direction. Overpass measurements occur in grids whose area varies from 13 km × 24 km (along × cross track, 312 km^2) at nadir to 13 km × 150 km (1,950 km^2) at the largest swath angle of 57°. Each swath angle is associated with a parameter named the cross track position (CTP). It ranges from 0 to 59 and corresponds to a grid of an OMI overpass measurement that refers to an earth's surface coordinate.

In the OMI algorithm, a grid can have cloudy and cloud-free parts. The cloudy part is proportional to CF and treated as a Lambertian surface to which an empirically adjusted albedo of 0.8 at 350 nm is associated. However, this part of the grid is taken as a pure reflector without transmitting or absorbing any radiation. The radiation transmission is referred only to the cloud-free part of the grid, compensating the missing transmission of a real cloud.

3 The routine for the determination of the local cloud cover

Fundamentally, there are three inconvenient effects associate with large ZA in the TSI images: (1) the perspective effect; (2) the image distortion yielded by the TSI mirror; and (3) the solar glare yielded by a significant aerosol load. A good way to reduce or be free from these effects is to cut the peripheral circular area of the TSI images out during processing. It means to pre-select a suitable image field of view (FOV) to obtain the processed images without a significant contribution from such effects, dismissing further procedural corrections to the cloud cover measurements. Image FOVs ranging from 100° to 160° have been adopted by authors using similar instruments (Kazantzidis et al. 2012; Kreuter et al. 2009; Long et al. 2006; Martins et al. 2003; Pfister et al. 2003; Sabburg and Long 2004).

However, reducing the image FOV means disregarding cloud cover information, and balance between cutting spurious effects out and keeping crucial cloud cover information must be achieved. Figure 1 depicts the cloud cover drawn from TSI images on April 10 2009 in BH for image FOVs from 40° to 160°. Images were obtained at a rate of 1 image per minute. First, note that cloud cover variations become smoother with the increase in the FOV and such an effect is caused by the decrease in the cloud cover variation in relation to the area embedded by the FOV considered. Secondly, clouds in the peripheral areas can lead to cloud cover values disconnected from the real sky scenario over and immediately surrounding the TSI set. This part of the sky is the most important one regarding the dependence of some geophysical parameters on local variations (Silva 2009, 2011). A good example lies in the 16:30–17:00 universal time (UT) period. The corresponding TSI images show a practically cloud-free sky above the TSI set and some cloudiness for ZA > 60°. The latter represents the ≈40 % cloud cover in the 160° image FOV frame (all clouds are included when using such a wide FOV), completely differing from the local reality which is better represented by the use of a smaller FOV like 100°. On the other hand, FOV apertures much smaller than this value produce unreal cloud cover values as depicted around 16:00 UT in the frame for 40° image FOV. This small FOV reveals just a 5 % cloudy sky, while it is around 50 % according to the visual inspection of the TSI images, indeed. In addition, clouds above the TSI set can easily be driven inward or outward of such a narrow FOV. A more realistic cloud cover is evidenced by a larger FOV like, again, that with 100° aperture. Thus, to avoid such opposite, extreme situations leading to false cloud cover, one must use an adequate FOV to obtain a detailed correspondence between the processed TSI images and the reality in the local sky. An adequate FOV results from the balance between cutting pixels for the necessary mitigation of effects associated with large ZA and keeping pixels to an amount capable of depicting a reliable scenario. A value between those extreme FOV performs the adequate aperture. Average cloud covers calculated for the 16–17 h UT period for each FOV aperture produce the values shown

internally on the right side of the frames in Fig. 1. They reach a minimum for images with FOV of 60°–100°. In addition, the smallest standard deviation in this group is obtained for 100°. This FOV seems to be the best aperture for the cloud cover determination as it contains more information than a 60° FOV without introducing significant amounts of the spurious effects of perspective and mirror distortion. Kassianov et al. (2005) obtained the same result based on the idealized considerations of cloud cover applied to a simulation code.

Each TSI image represents the cloud cover above and in the immediate surrounds of the TSI set at a given instant. However, the main goal in this study is to develop a routine to draw the cloud cover for a locality as much as possible free from spurious effects. For it, it is quite reasonable to assume that the same temporal average cloud cover is obtained at any point within an area under similar meteorological conditions. Many authors have used that principle to obtain the cloud cover for a given locality within some tens of minutes (Berendes et al. 2004; Gadhavi et al. 2008; Pfister et al. 2003; Sabburg and Long 2004). Hence, the obtained TSI images can be processed for a 100° FOV aperture then converted to temporal running averages. This procedure yields the local cloud cover (LCC). LCC is the average value of cloud cover addressed to the local conditions within a given time interval. Note that, this parameter differs from the classical cloud cover concept for taking into consideration only the local sky conditions within the 100° FOV of an image, and showing specific features for a particular coordinate with the capability of being applied to larger areas as an average.

The uncertainties in cloud cover measurements depend directly on the borderline between cloud and cloud-free sky. However, the precise identification of this region is not yet achievable due to the inaccuracy in the determination of borders and thin parts of clouds using the clear/thin and thin/opaque parameters. Therefore, we will assume (or accept) an uncertainty of at least 10 % in LCC (Jeong and Li 2010; Sabburg and Long 2004). On the other hand, since LCC is a temporal average, we can use its corresponding standard deviation as a measurement of the cloud cover variability (the LCC variability). This parameter brings information on the behavior and trends of cloud cover. Intuitively, it is reasonable to say that the LCC variability is proportional to (1) the cloud cover (here represented by LCC), and (2) the amount of cloud-free sky (100−LCC). Hence,

$$\begin{aligned} \mathrm{LCC}_{\mathrm{variablity}} &\propto \mathrm{LCC} \times (100 - \mathrm{LCC}) \\ &\propto 100\mathrm{LCC} - \mathrm{LCC}^2 \\ &= a + 100b\mathrm{LCC} - c\mathrm{LCC}^2, \end{aligned} \tag{1}$$

where a, b, and c are empirical coefficients for adjusting Eq. (1) to the experimental data. The LCC variability reflects the cloud dynamics influenced by meteorological (speed and direction of wind, humidity, pressure, temperature, clouds' altitude) and geophysical (amount and type of aerosols, sky illumination) aspects. However, the complexity of such influences is not fully represent by the simplicity and straightforwardness of Eq. (1), whose quadratic dependence on LCC only depicts general results like: (1) maximum LCC variability tends to occur for mid-range

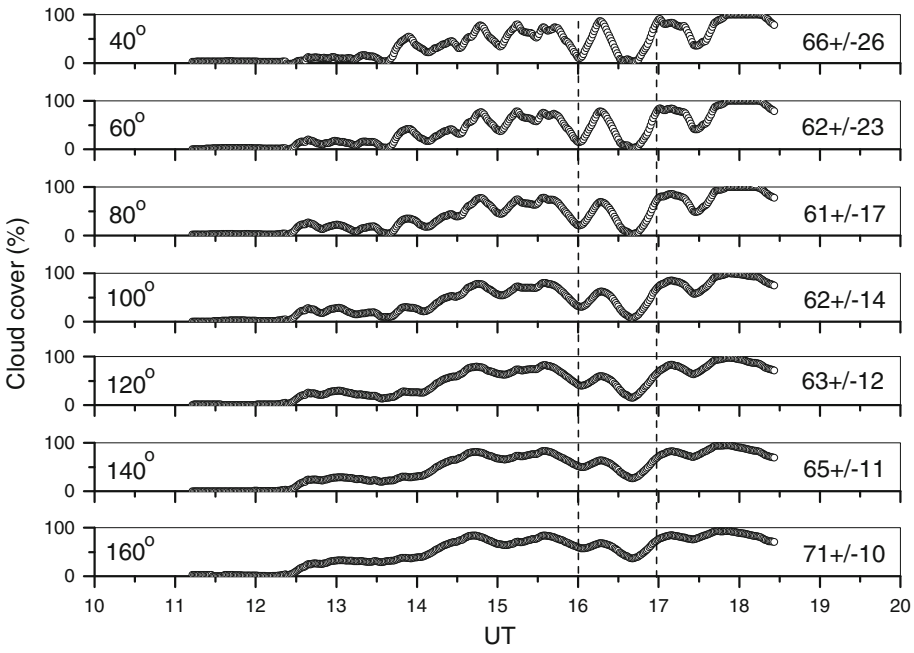

Fig. 1 Cloud cover in BH on April 10 2009. Figures inside the frames are (on the *left*) the FOV of TSI images and (on the *right*) the average cloud cover ±1 standard deviation for the 16–17 h period indicated by *vertical dashed lines*. Time is universal time (UT)

LCCs ($\approx$50 %); and (2) because the LCC variability depends on LCC, the probability density function associated with a set of instant cloud cover values leading to a given LCC is not necessarily normal (or Gaussian), tending to be skewed especially for extreme LCC values. Therefore, based on item 2, we must adopt Eq. (1) to obtain the standard deviation to be associated with an LCC value, since the use of a standard deviation drawn from the cloud cover values that lead to an LCC value could be unfit to this LCC under the point of view of normal distribution statistics.

4 Methodology

A TSI (#157) was setup in the campus of the Pontifícia Universidade Católica de Minas Gerais (PUC Minas) in BH by the Laboratório de Luz Ultravioleta (LLUV, http://www.dfq.pucminas.br/PUV/index.html). In the top of a tower, the imager had an almost free horizon with a few trees blocking some small parts of the sky at ZA $>$ 75°. Sky images were obtained at a rate of 1 image per minute within 11:00–19:00 UT (diurnal period). Around 480 images were released daily from September 2007 to November 2010. Interruptions in the TSI operation had occurred in January–March and September–November 2008 for operational maneuvers with the equipment. The TSI routine processed the TSI images yielding the corresponding cloud cover values for a 100° FOV aperture. Then they were converted into LCC values as to 60-min running averages, which represent hourly average cloud cover values calculated at a rate of 1 per minute. Hourly values of LCC are important to the cloud cover monitoring in meteorological applications. However, any other time lag for the calculation of LCC can be adopted depending only on the observer's discretion.

For comparison with CF data from OMI (OMI CF data available at avdc.gsfc.nasa.gov/index.php?site=1593048672&id=28), LCC was calculated as to 30-min running averages centered at the satellite overpass time. Although uncertainties in both longitude and latitude for the geolocation of the satellite grid are within 1 km (Kroon et al. 2008), a precise match with site's coordinates is needed to make useful comparisons with satellite data. Local boundary layer aspects like ground altitude, clouds, aerosols and surface albedo interfere in the satellite data (Berendes et al. 2004; Tanskanen et al. 2007). Thus, the center of the coordinates of a grid must be as close as possible to the center of coordinates of the site. In order to use only OMI overpass data referring precisely to BH, the BH territorial area of 331 km^2 was assumed as a circular area of 10.3 km radius with center at the coordinates of BH. Only satellite data whose grids have their center of coordinates within 10.3 km from the center of coordinates of BH (the OMI grid-BH distance) were picked up for comparison.

In terms of sky conditions, the International Commission on Illumination (CIE) has adopted 15 standards for sky representation (Li and Tang 2008). They span from overcast sky with steep luminance gradation towards zenith and azimuth uniformity to white blue, turbid sky with broad solar corona and such a range of classifications indicates not only a large variety of skies, but also the complexity associated with several mixed scenarios. Clouds, aerosols, and sky illumination perform a complicate and sometimes conjectural role to be identified, depicted, and analyzed. BH is a city with significant emission of pollutants to the atmosphere. In addition, a dry season extending for practically half a year reinforces the aerosol presence in the atmosphere. Therefore, a large variety of sky conditions are seen in the city. It means that both the clear/thin and thin/opaque parameters must suffer significant alterations to make the processed TSI images match the typical sky scene for a season.

5 Results and discussion

The application of the proposed routine to a single site for the determination of LCC does not represent any weaknesses to the general concept of the routine, since it (the routine) has been conceived as a general application without referring to any site's specificity.

5.1 LCC for BH

Three years of TSI operation yielded 7155 LCC values ranging from 0 to 100 %. Taking into consideration that LCC is an hourly average value, the depiction of it for long periods profiles a scrambled amount of information. To avoid this and provide a more informative data set, plots of LCC variability versus LCC with the quadratic curve of Eq. (1) are depicted in Fig. 2 for the four seasons. The scattering of points around the curve is produced by meteorological and geophysical aspects not taken into account by the equation and such aspects make each set of cloud cover values specific to a situation corresponding to a given LCC and its variability. Thus, it is reasonable to consider Eq. (1) as an average weighted curve regarding the cloud cover variability of LCC. An average LCC of 46 % was obtained for the full period of investigation and, as depicted in Table 1, LCC averages for fall, spring, and summer were 2.0, 2.3, and 3.0 times the winter value, respectively. Using Eq. (1) (whose coefficients a, b, and c are shown in Table 1) to calculate the LCC variability for these averages, we find 23 % for fall and spring, 19 % for

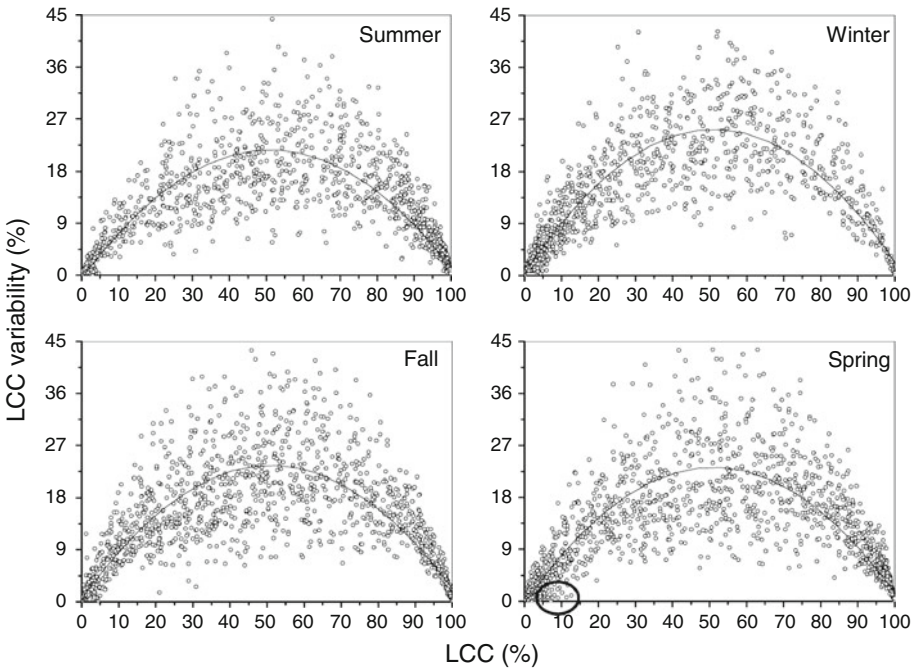

Fig. 2 Seasonal plots of LCC variability versus LCC for BH with the quadratic fitting *curve*

summer, and 18 % for winter. The occurrence of the lowest average LCC value (and, consequently, the lowest average LCC variability too) for winter reflects a drier scenario. The frame of Fig. 2 (for spring) shows a circumscribed area indicating a particular large number of exceptionally low LCC variability values. They correspond to the end of the dry season. There are at least two phenomena capable of inducing these data: (1) biomass burning smoke uses to accumulate in the region producing a stagnant atmosphere burdened by aerosols that hinder both formation and variation of clouds (Jones and Christopher 2008; Loeb and Schuster 2008); (2) in that season, mid and high altitude clouds are more frequent, and cloud size variations seem to be apparently smaller from the ground. Consequently, the LCC variability tends to be smaller.

Regarding the adjusted coefficients *a*, *b*, and *c*, a null value is ascribed theoretically to coefficient *a* in accordance with Eq. (1)'s development. However, this coefficient was significant (95 % of confidence against the null hypotheses) for winter, representing the incorporation of a systematic contribution to the LCC variability and such a contribution can be due to higher amounts of aerosols in the atmosphere in the dry season. However, in that case, the contribution would represent a contamination yielded probably by the difficulty to determine the borders and thin parts of clouds using the clear/thin and thin/opaque parameters, indeed. Coefficients *b* and *c* were well determined for all seasons with significant differences between winter and the other seasons. Similarly, except for summer and spring, the coefficient of determination (r^2) had statistically significant differences among all seasons with the highest value for winter. The percent scattering SD % to measure the scattering of points around each of the adjusted quadratic curves was not so large despite what Fig. 2 suggests. SD % values were similar among the seasons ranging from 9 % in winter to 12 % in fall. The first outcome from these results is that Eq. (1) (and its parameters) has seasonal dependence. The second outcome is that Eq. (1) can work as a backbone for several other mathematical expressions to be added to it in an attempt to

Table 1 Data referring to plots in Fig. 2: averages LCC

Season	LCC (%)	Eq. (1)'s coefficients			r^2	SD %	N
		a	b	c			
Summer	68	-0.547 ± 0.359	$(0.870 \pm 0.016) \times 10^{-2}$	$(0.852 \pm 0.013) \times 10^{-2}$	0.76	10	1,509
Fall	46	0.477 ± 0.247	$(0.905 \pm 0.013) \times 10^{-2}$	$(0.886 \pm 0.013) \times 10^{-2}$	0.74	12	1,679
Winter	23	0.295 ± 0.110	$(0.975 \pm 0.009) \times 10^{-2}$	$(0.954 \pm 0.011) \times 10^{-2}$	0.85	9	2,018
Spring	54	-0.285 ± 0.215	$(0.921 \pm 0.012) \times 10^{-2}$	$(0.903 \pm 0.011) \times 10^{-2}$	0.77	11	1,949

a, *b*, and *c* coefficients for Eq. (1); coefficient of determination r^2; percent scattering SD %; and N data points. Uncertainties are 1σ

Table 2 Time-dependent monthly average LCC (%) for BH

	11–12	12–13	13–14	14–15	15–16	16–17	17–18	18–19
SEP2007	23	27	27	24	21	19	17	23
OCT2007	38	38	33	39	35	42	48	55
NOV2007	68	63	73	73	74	64	64	58
DEC2007	45	51	56	64	60	61	62	70
APR2008	27	29	30	46	49	52	51	53
MAY2008	14	19	24	33	42	46	38	36
JUN2008	11	10	13	22	27	33	31	36
JUL2008	11	11	11	8	6	9	10	12
AUG2008	19	9	8	7	11	14	13	18
DEC2008	77	84	85	83	87	86	82	84
JAN2009	64	64	66	80	77	67	74	67
FEB2009	50	60	61	62	74	68	71	68
MAR2009	50	50	54	68	77	67	64	70
APR2009	34	42	49	62	63	61	64	61
MAY2009	28	23	30	37	38	40	46	46
JUN2009	30	25	32	34	41	41	44	38
JUL2009	20	19	22	20	28	35	34	37
AUG2009	36	39	38	36	40	43	46	51
SEP2009	30	34	35	39	47	54	53	57
OCT2009	56	63	65	66	68	77	79	76
NOV2009	52	54	66	93	73	47	56	68
DEC2009	74	68	73	90	96	80	79	82
JAN2010	44	48	61	83	86	63	64	68
FEB2010	38	42	45	72	77	55	56	61
MAR2010	48	56	57	63	63	65	60	60
APR2010	28	30	39	44	48	51	51	53
MAY2010	29	37	45	45	49	46	49	41
JUN2010	23	24	29	25	23	23	23	24
JUL2010	23	22	24	25	26	27	30	29
AUG2010	3	9	9	5	5	6	4	5
SEP2010	37	38	35	29	30	31	35	34
OCT2010	67	65	67	80	69	63	62	64
NOV2010	80	84	90	90	85	80	77	74

Time interval in UT

explain quantitatively the LCC variability in terms of other meteorological and geophysical aspects.

Time-dependent monthly average LCC values are depicted in Table 2, where large variations can be identified among the 33 months of measurements. LCC varied from a minimum 3 % at 11–12 h UT in August 2010 (AUG2010) to a maximum 96 % at 15–16 h UT in December 2009 (DEC2009). The LCC variability for these LCC values using Eq. (1) are 3 and 4 %, respectively and such results clearly reflect the weather scenario of rainy (DEC2009) and dry (AUG2010) seasons. Correspondingly, Fig. 3 shows time-dependent seasonal average LCC values for the diurnal evolution of LCC. In general, LCC values increased diurnally, except for spring that showed an LCC of approximately 54 %. Winter showed the lowest LCCs, while summer did the highest values, especially at the 15–16 h UT interval (noon time at 15 h UT) with a peak clearly set at noon. This peak results from the lifting of rainy season's humidity by warm parcels of air in the summer's hot weather, leading to the systematic development of huge masses of clouds in the hottest periods of the day. Fall and spring showed similar LCCs in the afternoons, but in the mornings the former tended to show lower values than the latter. The LCC variability for these seasonal LCCs can be obtained from Eq. (1). All these differences in LCC indicate seasons that are well delimited and featured.

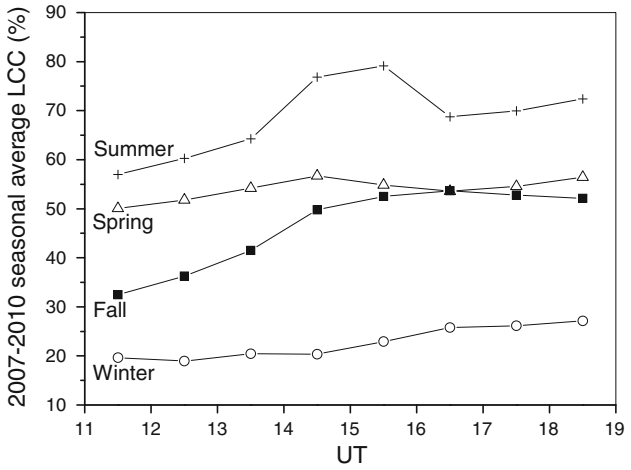

Fig. 3 Time-dependent seasonal averages of LCC in BH

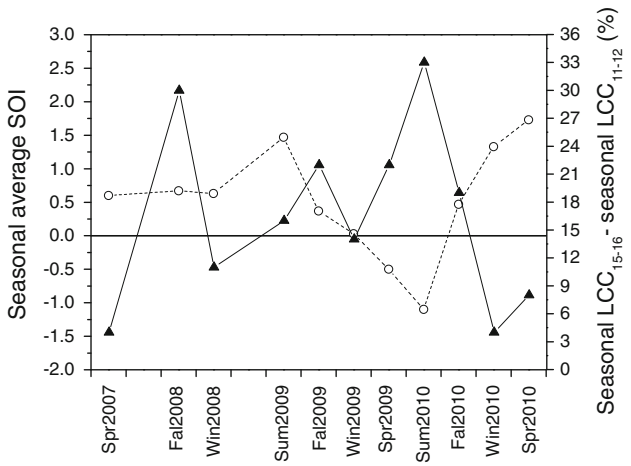

Fig. 4 *Empty circles* with a *dashed line* represent the seasonal average SOI, while *full black triangles* with a *solid line* do the difference between noon and early morning seasonal LCC for BH along the 2007–2010 period

The sky scenario in BH varies significantly especially due to the presence of particle matter in the atmosphere. Consequently, the clear/thin parameter in the TSI routine had to be varied in the range of 0.4–0.9 (or 40–90 % in accordance with the TSI routine terminology) in this study. Hence, there are considerable uncertainties set in for LCC. A deep and detailed approach is needed in relation to these uncertainties, but they are quite complex to be fully investigated here. The use of pixel parameters based on the R/B ratio by the TSI routine can lead to mistakes caused by aerosol plumes exposed to the sunlight that match cloud characteristics and make unclear the cloud-aerosol borderline. Some investigators have assessed other methodologies based on the textural characteristics of an image to identify clouds and to determine the cloud cover. Such a procedure can provide better differentiation between clouds and aerosols, and identify clouds in terms of species in addition to genera (Calbó and Sabburg 2008; Heinle et al. 2010; Kreuter et al. 2009; Wang et al. 2010).

5.2 LCC and ENSO

For all seasons, the largest variations in LCC occur typically between early morning (11–12 h UT) and noon (15–16 h UT). This is especially true for fall and summer as Fig. 3 clearly depicts. However, that variation can have a contribution from ENSO. ENSO is a quasi-periodic pattern in climate across the tropical zone of the Pacific Ocean (Neelin and Latif 1998). It is roughly a 3–7 year period characterized by variations in the ocean's surface temperature. For the west coast of South America, warming and cooling features El Niño and La Niña respectively. Both events produce significant changes in weather and climate across the world. However, a detailed explanation of the phenomenon is still on study. There is a pool of signs alerting for ENSO. The atmospheric pressure difference between Tahiti and Darwin is one of them, It is known as the Southern Oscillation Index (SOI, http://www.cpc.ncep.noaa.gov/data/indices/soi). SOI negative values indicate warming of ocean waters producing an increase in precipitation for many parts of South America (Souza-Echer et al. 2008). It means an increase in the cloud cover too. The cooling of ocean waters produces an inverse effect.

Figure 4 depicts both the seasonal average SOI and the difference between noon and early morning seasonal average LCC in BH for the period of investigation. There is no link apparent between LCC and SOI from spring 2007 (Spr2007) to fall 2009 (Fal2009). However, an augmentation in LCC around noon was significant for spring 2009 (Spr2009), summer 2010 (Sum2010), and early fall 2010 (Fal2010), while a reduction occurred for part of fall 2010 (Fal2010), winter 2010 (Win2010), and spring 2010 (Spr2010) (See Table 2; Fig. 3 for comparison between early morning and noon values). Apparently, there is an antagonistic link between LCC and SOI perfectly corresponding to an ENSO event in 2009–2010. In fact, 2009–2010 and 2010–2011 were El Niño and La Niña periods respectively (Boening et al. 2012). Correspondingly, DEC2009 and AUG2010 had, respectively, the highest and lowest time-dependent monthly average LCC values in this investigation. Figure 5 shows linear fittings applied to the seasonal data of LCC versus SOI for two periods. The first period Spr2007—winter 2009 (Win2009) was a non-ENSO period for which both poor correlation coefficient $r = 0.03$ and large SD % = 39 % were obtained. A totally different scenario was obtained for the second period from Spr2009 to Spr2010, which corresponds to an ENSO period. For it, the linear fitting yielded $r = -0.95$ (95 % confidence level for rejection of null

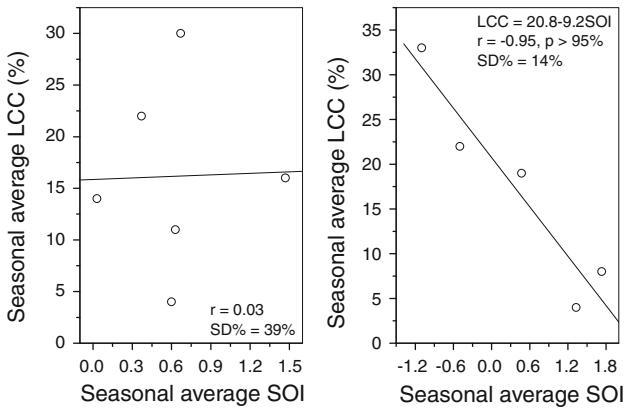

Fig. 5 Linear fitting of LCC versus SOI (seasonal averages): (*left*) for the Spr2007–Win2009 period; and (*right*) for the Spr2009–Spr2010 period

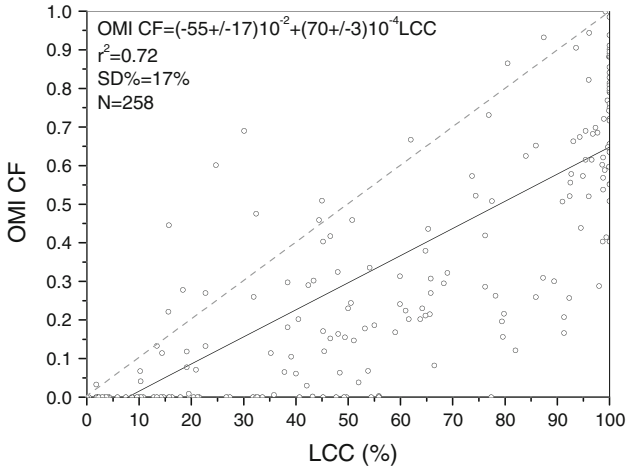

Fig. 6 OMI CF versus LCC for BH. The *dashed line* bisects the frame. Uncertainties are 1σ

hypothesis regarding $r \approx 0$), SD % = 14 %, and the relation $\mathrm{LCC} = (20.8 \pm 2.0) + (-9.2 \pm 1.8)\mathrm{SOI}$ was obtained between the seasonal averages of LCC and SOI. These results suggest a link between LCC and ENSO through SOI. However, any interpretation from these results must be seen cautiously due to the shortness of the data series.

5.3 LCC and OMI CF

Although OMI measurements refer to a relatively small atmospheric area, yet that area is large in comparison with that embedded by ground-based instruments, such as TSI. Not surprisingly, large differences can appear in the comparison between satellite and ground-based data. The satellite parameter of CF is a flat view of the atmosphere through a two-dimentional algorithm, while the LCC sounds more like a 3-dimensional hemispherical real view of the atmosphere from a ground-based instrument. In addition, although TSI is sensitive to the cloud positioning within the instrument's FOV, the OMI algorithm releasing CF is not sensitive to the cloud positioning within the grid of satellite data.

An OMI CF versus LCC linear fitting is shown in Fig. 6 for 258 OMI overpass measurements. They comply with the restriction of OMI grid-BH distance ≤10.3 km. In this case, the average OMI grid-BH distance was 6.0 km, the average CTP was 26, the site's altitude ranged from 801 to 1,205 m a.s.l. averaging 930 m, and the OMI overpass time ranged from 16:00 to 17:44 UT averaging 16:52 UT. OMI CF typically underestimates the cloud cover in relation to LCC values as there are many pairs of both $\mathrm{LCC} = 100\ \% \times \mathrm{OMI\ CF} < 1$ and $\mathrm{LCC} \neq 0 \times \mathrm{OMI\ CF} = 0$. Apparently, the main reason for that comes from the fact that the 3-dimensional hemispherical view of cloud cover produced by TSI shows more from local clouds than the 2-dimensional flat view produced by the satellite algorithm. On the other hand, the satellite view shows more from the atmosphere than the ground-based imager does. Since the average LCC for the whole period of investigation was 46 %, it seems reasonable to think of the atmosphere as a place that tends to be cloud-free, what justifies the trend towards lower cloud cover values from OMI CF in relation to LCC.

The linear fitting yielded $r^2 = 0.72$ and SD % = 17 %, although the apparent large scattering of points around the fitting line. As a matter of reference, CF data from 1 km^2 grid area (at nadir) measured by the moderate resolution imaging spectrometer (MODIS) experiment on board the Aqua satellite by NASA (Schoeberl et al. 2004) yielded $r^2 = 0.84$ when compared with OMI CF (Stammes et al. 2008). As already mentioned before, the grid area for an OMI measurement depends on CTP. An analysis of the CTP distribution corresponding to the present OMI CF data gives 169 measurements with CTP ≤ 26. Using only these 169 OMI CF data for another OMI CF *vs* LCC linear fitting produces $r^2 = 0.71$ and SD % = 17 %. Comparing with the results from Fig. 6, it means the increase in OMI grid areas with CTP (equivalently, the decrease in resolution) does not represent a significant reduction in the quality of the OMI CF versus LCC comparison. In fact, a more important item here is to ensure that both satellite grid and site have similar center of coordinates, what is a guarantee that the information in the satellite grid corresponds to the geophysical and meteorological condition at the aimed site. This is obtained through the restriction of OMI grid-BH distance ≤10.3 km, which is a fundamental tool to pick up appropriate satellite data for a site. Therefore, the occurrence of satellite data with large CTP does not depreciate the comparison between CF and LCC in this case.

6 Conclusions

The routine presented in this study determined the cloud cover through the LCC parameter obtained from TSI images. LCC corresponds to a temporal average from a set of instantaneous cloud cover values within a zenith centered angle of 100° FOV. The LCC variability within a time interval depends on LCC. It can be obtained by Eq. (1) as a value weighted by geophysical and meteorological aspects influencing LCC. In addition, the seasonality apparent in Eq. (1) brings important information regarding both LCC and LCC variability. The TSI data are based on the R/B ratio of an image pixel, which presents a significant dependence not only on clouds but also on atmospheric contents like aerosols and sky illumination. The proposed routine showed proper results in the determination of cloud cover for an urban, tropical site. Application to other sites with different climatology is encouraged to test the applicability of the proposed routine widely.

In the 2007–2010 period, the average LCC for BH was 46 %. Monthly average values varied from 3 % in the dry season to 96 % in the rainy one. Seasons were well delimited and featured in terms of LCC. Summer showed the largest seasonal average LCC of 68 % followed by spring 54 %, fall 46 %, and winter with 23 %. In addition, summer also showed an LCC peak of 79 % around noon. Fall and spring had very similar afternoon LCC ($\approx$50 %), but the former presented lower values in the mornings. The lowest seasonal average LCC of 19 % occurred in winter at 12–13 h UT.

The 2009–2010 seasonal average LCC seems to be coupled with ENSO. In fact, the variation in LCC between noon and early morning showed a statistically significant link with SOI through LCC = (20.7 ± 2.0) + (−9.2 ± 1.8)SOI, $r = -0.95$, and SD % = 14 %. However, the use of a larger data series (maybe a few decades of ground or satellite data) for such a comparison is recommended before any further rigorous interpretation.

A comparison of LCC (averaged for 30 min) to OMI CF showed a fair $r^2 = 0.72$. In addition, satellite CF data tended to lower values of cloud cover in relation to ground-based LCC and such a difference was already expected due to conceptual differences between these parameters. Consequently, satellite CF data can be unable to show eventual cloud cover aspects with the same property and precision as the ground-based LCC for a specific site.

To sum up, the LCC parameter yielded by the proposed routine shows a symptomatic correspondence with cloud cover for time intervals from tens of minutes to seasons, satellite data, and, possibly, natural events like ENSO. LCC is a worthy indicator of the cloud cover scenario based on the information obtained from one specific point within a locality.

Acknowledgments This study was financially supported by Conselho Nacional de Desenvolvimento Científico e Tecnológico (CNPq, Grants 471159/2004-2, 300162/2012-0, and other grants), Fundação de Amparo à Pesquisa do Estado de Minas Gerais (FAPEMIG, CRA APQ 0848-5.02/07), and logistic supported by PUC Minas.

References

Berendes TA, Berendes DA, Welch RM, Dutton EG, Uttal T, Clothiaux EE (2004) Cloud cover comparison of the MODIS daytime cloud mask with surface instruments at the north slope of Alaska ARM site. IEEE Trans Geosci Remote Sens 42:2584–2593

Boening, C, Willis JK, Landerer FW, Nerem RS, Fasullo J (2012) The 2011 La Niña: so strong, the oceans fell. Geophys Res Lett 39. doi:10.1029/2012GL053055

Calbó J, Sabburg J (2008) Feature extraction from whole-sky ground-based images for cloud-type recognition. J Atmos Oceanic Technol 25:3–14. doi:10.1175/2007JTECHA959.1

Carslaw KS, Harrison RG, Kikby J (2002) Cosmic rays, clouds, and climate. Science 298:1732–1736

Cazorla A, Olmo FJ, Alados-Arboledas L (2008) Development of a sky imager for cloud cover assessment. J Opt Soc Am A 25:29–39

Chiu JC, Marshak A, Knyazikhin Y, Pilewski P, Wiscombe WJ (2009) Physical interpretation of the spectral radiative signature in the transition zone between cloud-free and cloudy regions. Atmos Chem Phys 9:1419–1430

Gadhavi H, Pinker RT, Laszlo I (2008) Estimates of surface ultraviolet radiation over North America using Geostationary Operational Environmental Satellites observations. J Geophys Res 113:D21205. doi:10.1029/2007JD9308

Heinle A, Macke A, Srivastav A (2010) Automatic cloud classification of whole sky images. Atmos Meas Techol 3:557–567

Hobbs PV (1993) Aerosol-cloud-climate interactions. In: International geophysical series 54, Academic Press, San Diego

Holle RL, MacKay SA (1975) Tropical cloudiness from all-sky cameras on Barbados and adjacent Atlantic Ocean. J Appl Meteorol 14:1437–1450

Houze RA Jr (1993) Cloud Dynamics. Academic Press, San Diego

Jeong M-J, Li Z (2010) Separating real and apparent effects of cloud, humidity, and dynamics on aerosol optical thickness near cloud edges. J Geophys Res 115:D00K32. doi:10.1029/2009JD013547

Jones TA, Christopher SA (2008) Seasonal variation in satellite-derived effects of aerosols on clouds on the Arabian Sea. J Geophys Res 113:D09207. doi:10.1029/2007JD009118

Kassianov E, Long CN, Ovtchinnikov M (2005) Cloud sky cover versus cloud fraction: whole-sky simulations and observations. J Appl Meteorol 44:86–98

Kazantzidis A, Tzoumanikas P, Bais AF, Fotopoulos S, Economou G (2012) Cloud detection and classification with the use of whole-sky ground-based images. Atmos Res 113:80–88. doi:10.1016/j.atmosres.2012.05.005

Kiehl JT (1994) Clouds and their effects on the climate system. Phys Today 11:36–42

Koren I, Remer LA, Kaufman YJ, Rudich Y, Martins JV (2007) On the twilight zone between clouds and aerosols. Geo Res Lett 34:L08805. doi:10.1029/2007GL029253

Kreuter A, Zangerl M, Schwarzmann M, Blumthaler M (2009) All-sky imaging: a simple, versatile system for atmospheric research. Appl Opt 48:1091–1097

Kroon M, Dobber MR, Dirksen R, Veefkind JP, van den Oord GHJ, Levelt PF (2008) Ozone Monitoring Instrument geolocation verification. J Geophys Res 113:D15S12. doi:10.1029/2007JD008821

Levelt PF, van den Oord GHJ, Dobber MR, Mälkki A, Visser H, de Vries J, Stammes P, Lundell JOV, Saari H (2006) The Ozone Monitoring Instrument. IEEE Trans Geosci Remote Sens 44:1093–1101

Li DHW, Tang HL (2008) Standard skies classification in Hong Kong. J Atmos S-Terres Phys 70:1222–1230

Loeb NG, Schuster GL (2008) An observational study of the relationship between cloud, aerosol and meteorology in broken low-level cloud conditions. J Geophys Res 113:D14214. doi: 10.1029/2007JD009763

Long CN (2010) Correcting for circumsolar and near-horizon errors in sky cover retrievals from sky images. Open Atmos Sci J 4:45–52

Long CN, Sabburg JM, Calbó J, Pagès D (2006) Retrieving cloud characteristics from ground-based daytime color all-sky images. J Atmos Ocean Technol 23:633–652

Mantelli Neto SL, Wangenheim AV, Pereira EB, Comunello E (2010) The use of Euclidean geometric distance on RGB color space for classification of sky and cloud patterns. J Atmos Ocean Technol 27:1504–1517

Martins FR, Souza MP, Pereira EB (2003) Comparative study of satellite and ground techniques for cloud cover determination. Adv Space Res 32:2275–2280

Mason BJ (1972) The Physics of Clouds. Clarendon Press, Oxford

McKenzie RL, Aucamp PJ, Bais AF, Björn LO, Llyas M, Madronich S (2011) Ozone depletion and climate change: impacts on UV radiation. Photochem Photobiol Sci 10:182–198. doi:10.1039/C0PP90034F

Neelin JD, Latif M (1998) El Niño dynamics. Phys Today 51:32–36

Pfister G, McKenzie RL, Liley JB, Thomas A, Forgan BW, Long CN (2003) Cloud coverage based on all-sky imaging and its impact on the surface solar irradiance. J Appl Meteorol 42:1421–1434

Sabburg JM, Long CN (2004) Improved sky imager for studies of enhanced UV irradiance. Atmos Chem Phys 4:2543–2552

Salby ML (1996) Fundamentals of atmospheric physics. In: International geophysical series 61. Academic Press, San Diego

Schoeberl MR, Douglas AR, Hilsenrath E, Bhartia PK, Barnett J, Gille J, Beer R, Gunson M, Waters J, Levelt PF, Decola P (2004) Earth observing system missions benefit atmospheric research. EOS 85:177–184

Silva AA (2009) Daily distribution of UV-Index in Belo Horizonte (Brazil) and the shadow rule. Revista Brasileira de Geofísica 27:313–322

Silva AA (2011) Local cloud cover, ground-based and satellite measurements of erythemal dose rate for an urban, tropical site in Southern Hemisphere. J Atmos S-Terres Phys 73:2474–2481. doi:10.1016/j.jastp.2011.09.002

Singh AK, Siingh D, Singh RP (2011) Impact of galactic cosmic rays on Earth′s atmosphere and human health. Atmos Environ 45:3806–3818

Souza-Echer MP, Pereira EB, Bins LS, Andrade MAR (2006) Simple method for the assessment of the cloud cover state in high latitude regions by a ground based digital camera. J Atmos Ocean Technol 23:437–447

Souza-Echer MP, Echer E, Nordemann DJR, Rigozo NR, Prestes A (2008) Wavelet analysis of a centennial (1895–1994) southern Brazil rainfall series. Clim Chang 87:489–497

Stammes P, Sneep M, de Haan JF, Veefkind JP, Wang P, Levelt PF (2008) Effective cloud fractions from the Ozone Monitoring Instrument: Theoretical framework and validation. J Geophys Res 113:D16S38. doi:10.1029/2007JD008820

Tanskanen A et al (2007) Validation of daily erythemal doses from Ozone Monitoring Instrument with ground-based UV measurement data. J Geophys Res 112:D24S44. doi:10.1029/2007JD008830

Wang Q, Liang J, Hu Z-J, Hu H-H, Zhao H, Hu H-Q, Gao X, Yang H (2010) Spatial texture based automatic classification of dayside aurora in all-sky images. J Atmos S-Terres Phys 72:498–508. doi:10.1016/j.jastp.2010.01.011